

Abell 370 revisited: refurbished Hubble imaging of the first strong lensing cluster

J. Richard^{1*}, J.-P. Kneib², M. Limousin^{2,3}, A. Edge¹, E. Jullo⁴

¹*Institute for Computational Cosmology, Department of Physics, Durham University, South Road, Durham, DH1 3LE, UK*

²*Laboratoire d'Astrophysique de Marseille, CNRS- Université Aix-Marseille, 38 rue Frédéric Joliot-Curie, 13388 Marseille Cedex 13, France*

³*Dark Cosmology Centre, Niels Bohr Institute, University of Copenhagen, Juliane Maries Vej 30, 2100 Copenhagen, Denmark*

⁴*Jet Propulsion Laboratory, Caltech, MS 169-327, Oak Grove Dr, Pasadena CA 91109, USA*

Accepted 2009 November 27. Received 2009 November 27; in original form 2009 October 29.

ABSTRACT

We present a strong lensing analysis of the galaxy cluster Abell 370 ($z=0.375$) based on the recent multicolor ACS images obtained as part of the Early Release Observation (ERO) that followed the Hubble Service Mission #4. Back in 1987, the giant gravitational arc ($z = 0.725$) in Abell 370 was one of the first pieces of evidence that massive clusters are dense enough to act as strong gravitational lenses. The new observations reveal in detail its disklike morphology, and we show that it can be interpreted as a complex five-image configuration, with a total magnification factor of 32 ± 4 . Moreover, the high resolution multicolor information allowed us to identify 10 multiply imaged background galaxies.

We derive a mean Einstein radius of $\theta_E = 39 \pm 2''$ for a source redshift at $z = 2$, corresponding to a mass of $M(< \theta_E) = 2.82 \pm 0.15 \times 10^{14} M_\odot$ and $M(< 250 \text{ kpc}) = 3.8 \pm 0.2 \times 10^{14} M_\odot$, in good agreement with Subaru weak-lensing measurements. The typical mass model error is smaller than 5%, a factor 3 of improvement compared to the previous lensing analysis. Abell 370 mass distribution is confirmed to be bi-modal with very small offset between the dark matter, the X-ray gas and the stellar mass. Combining this information with the velocity distribution reveals that Abell 370 is likely the merging of two equally massive clusters along the line of sight, explaining the very high mass density necessary to efficiently produce strong lensing.

These new observations stress the importance of multicolor imaging for the identification of multiple images which is key to determining an accurate mass model. The very large Einstein radius makes Abell 370 one of the best clusters to search for high redshift galaxies through strong magnification in the central region.

Key words: Gravitational lensing - Galaxies: clusters: general - Galaxies: clusters: individual (A370)

1 INTRODUCTION

The discovery of the “giant luminous arcs” in rich clusters of galaxies in the mid-80’s (Lynds & Petrosian 1986; Soucail et al. 1987) has opened a new window of research in cosmology: gravitational lensing. This simple geometric tool allows to map out dark matter in the Universe on various angular scales. The strong lensing regime occurs in the densest part of galaxies and massive clusters. When a background source is straddling one or more caustic lines, giant luminous arcs can be produced. The identification of

multiple images has remained difficult until deep multicolor space-based imaging has become routinely possible. This has been effectively the case with the installation of the Advanced Camera for Surveys (ACS) aboard *Hubble* in March 2002. ACS observations of lensing clusters have lead to many discoveries of tens of multiple images (A1689: Broadhurst et al. 2005, Limousin et al. 2007; A1703: Limousin et al. 2008, Richard et al. 2009a; RXJ1347: Bradač et al. 2008a; the bullet cluster: Bradač et al. 2006; A2218: Elíasdóttir et al. 2007; C10024+1654: Zitrin et al. 2009; MS1358: Swinbank et al. (2009); MACS clusters: Zitrin & Broadhurst 2009, Smith et al 2009, Limousin et al 2010). These discoveries have foster the development

* Marie-Curie fellow. E-mail: johan.richard@durham.ac.uk

of new mass modeling techniques (e.g. Jullo et al. 2007, Coe et al. 2008, Jullo & Kneib 2009) that take advantage of the numerous constraints coming from these many multiple images. The accuracy of the best mass model is now approaching the percent level allowing: (1) the use of massive clusters lenses as probes of cosmography – hence putting strong geometrical constraints on the cosmological model (Golse & Kneib 2002, Soucail et al. 2004, Jullo & Kneib 2009), (2) recovering the intrinsic shape of lensed galaxies (Swinbank et al. 2009), and (3) accurate correction of the magnification and dilution effect of massive clusters to constrain the luminosity function of distant galaxies (e.g. Richard et al. 2008, Bouwens et al. 2009).

The ACS failure in January 2007 has stopped the observation and detailed analysis of further massive clusters. The recent recovery of the ACS camera last May 2009 now brings new opportunities to further investigate massive cluster lenses. We present in this letter a strong lensing analysis of the multicolor cluster observations obtained on Abell 370 as part of the Early Release Observation validating the performance of the repaired ACS instrument (Sect. 2). The identification of 10 multiply imaged background galaxies (hereafter called systems of multiple images) totaling 32 images and the lens modeling are presented in Sect. 3. The results on the nature of the giant arc and the mass distribution and substructure are presented in Sect 4.

Throughout the paper, we use magnitudes quoted in the AB system, and a standard Λ -CDM model with $\Omega_m = 0.3$, $\Omega_\Lambda = 0.7$, and $H_0 = 70 \text{ km s}^{-1} \text{ Mpc}^{-1}$, whenever necessary. $1''$ on the sky is equivalent to a physical distance of 5.16 kpc at the redshift $z = 0.375$ of the galaxy cluster.

2 OBSERVATIONS AND DATA REDUCTION

The HST/ACS observations were obtained in July 2009 (PID 11507, PI: Noll), for a total of 6780/2040/3840 sec in the F475W/F625W/F814W bands, respectively. We make use of the images provided by STScI, reduced using the package *multidrizzle*, and we measure AB depths (3σ) of 28.39/27.41/27.84 for a point source. The astrometry of these images was checked using the USNO optical catalogs.

We performed a visual inspection of the images to search for multiply lensed background galaxies. We made use of previous strong-lensing work by Kneib (1993), Smail et al. (1996) and Bézecourt et al. (1999) to guide our multiple image identification. Compared to the single WFPC2 observations in F625W, the new multicolor ACS data is deeper and has higher resolution. We identify 10 secure systems of images, including 6 new confirmed systems compared to previous lensing analyses (e.g. Abdelsalam et al. 1998), which we present in Fig. 1 and Table 1. We confirm that all these images are genuine by reproducing their positions and shape using the constructed lens model (Sect. 3) and by checking that their ACS colors agree within the 1σ error bar (Table 1). We use the notation $\alpha.\beta$ to design image β of system α . Two of these systems (1 and 2) have spectroscopic redshifts published by Soucail et al. (1988) and Kneib et al. (1993). Seven systems (all except 2, 7 and 10) are tangential systems of 3 images, while systems 7 and 10 are two radial arcs. We identify 5 images in total for system 7, but system 10 has a much lower surface brightness and we can not iden-

tify its counter-images securely. System 2 is the giant arc first identified by Soucail et al. (1987), and is a lensed image of a spiral galaxy. Thanks to the new multicolor images we identify 5 images of the central red bulge, while individual star-forming regions are recognized as triple images with blue colors (Fig. 1).

An 88 ksec *Chandra* ACIS observation was obtained in October 1999 as part of the program PID 525 (PI: Garmire). We used the adaptively smoothing algorithm *csmooth* in the CIAO package (Ebeling et al. 2006) on the events file with a maximum scale of $15''$. The astrometry of the X-ray data was checked using two bright isolated X-ray point sources located in the ACS image, and is better than $0.5''$.

3 STRONG-LENSING ANALYSIS

We have used *Lenstool*¹ (Kneib 1993; Jullo et al. 2007) to perform a mass reconstruction of the cluster, assuming a parametric model for the distribution of dark matter. This model was constrained using the location of all multiple images identified. This technique builds on the work done in Kneib et al. (1996), Smith et al. (2005) and Richard et al. (2009b), by describing the cluster mass distribution with a superposition of analytic mass components to account for both cluster- and galaxy-scale mass. For each component we use a dual pseudo-isothermal elliptical mass distribution (dPIE, also known as a truncated PIEMD, Elíasdóttir et al. 2007). The dPIE profile is characterized by its central position (α, δ) , position angle (θ) , ellipticity (e) , fiducial velocity dispersion σ_0 and two characteristic radii: a core radius r_{core} and a cut-off radius r_{cut} . Galaxy-scale mass components are added at the location of galaxies color-selected from the cluster red sequence. In order to limit the number of free parameters, the velocity dispersion, cut-off radius and core radius is scaled to the galaxy luminosity L , relative to the luminosity of a L^* galaxy (see Jullo et al. 2007, for details). We fix $r_{\text{core}}^* = 0.15 \text{ kpc}$ and $r_{\text{cut}}^* = 45 \text{ kpc}$ to prevent degeneracies between the different parameters (see also Limousin et al. 2007 and Richard et al. 2009b for a discussion of these parameters). We kept σ_0^* as a free parameter. Finally, the unknown redshifts of systems 3 to 9 are kept as free parameters. The faint surface brightness of the northern radial arc (System 10) and the absence of counter-images do not allow us to include it as a constraint.

The model is optimized with the Bayesian Markov chain Monte-Carlo (hereafter MCMC) sampler, described in detail in Jullo et al. (2007). The mass distribution is optimized by minimising the distance between the positions of the multiple images unlensed back to the source plane. We used the image-plane root mean squared (RMS) distance σ_i of the images predicted by the model to the observed positions as an accuracy estimator of the model (Limousin et al. 2007).

A model including a single cluster-scale component, such as the one used in the early analysis by Bergmann et al. (1990), largely fails in reproducing the multiple constraints ($\sigma_i \sim 3.5''$). This result was already pointed out by Kneib et al. (1993), who showed that the locations and curvature radii of the arcs and multiple images (in particular

¹ Publically available, see <http://www.oamp.fr/cosmology/lenstool> to download the latest version

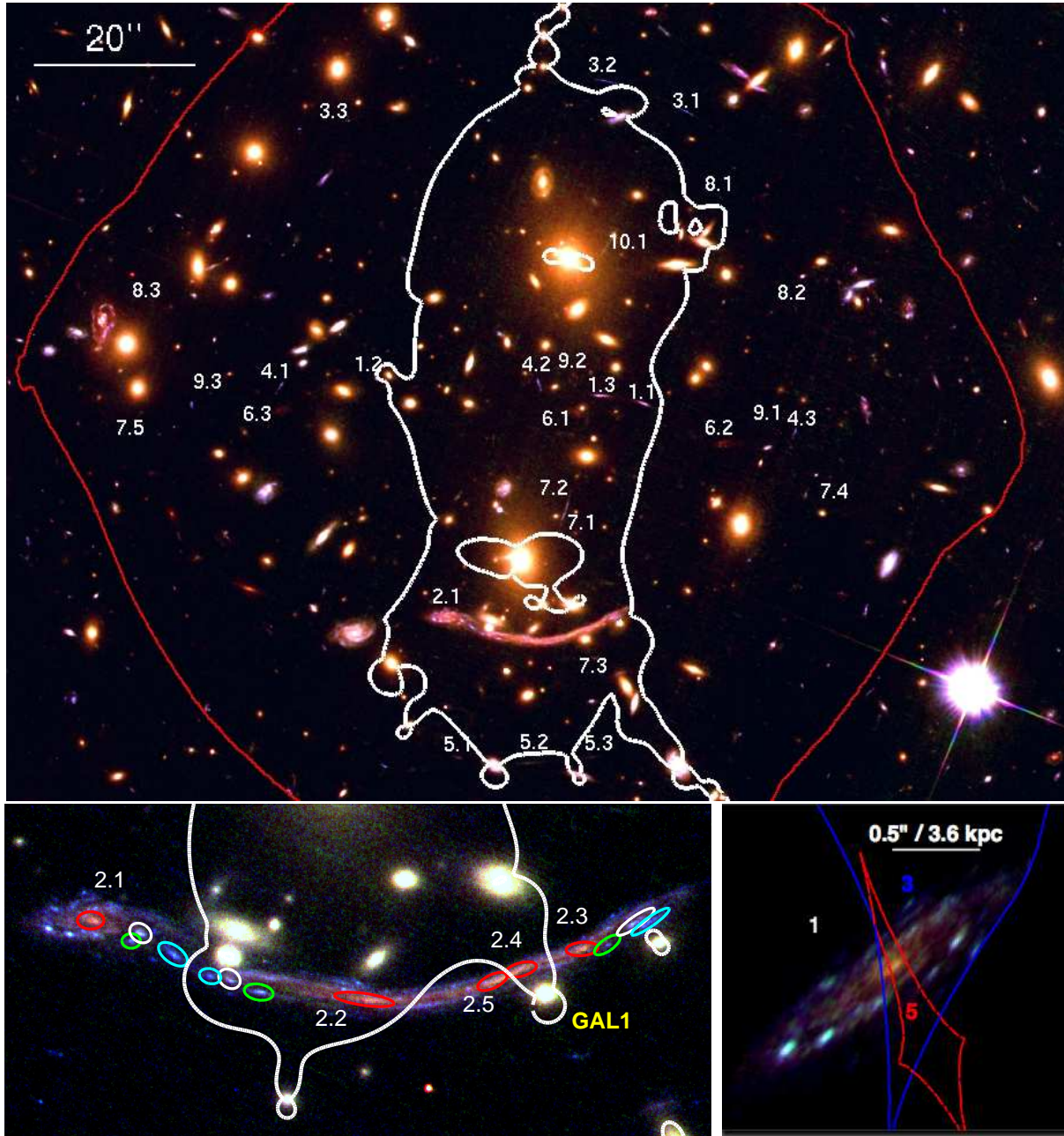


Figure 1. (Top panel) ACS F475W/F625W/F814W color image showing the location of the identified multiple systems, along with the critical line at $z=1.2$ (redshift for the majority of the multiple images). The red line delimits the region of multiple images for very high redshift sources (here assuming $z = 6$). (Bottom panels) System 2: Location of matched regions (identified with colored ellipses) in each part of the giant arc. The white line shows the critical curve at $z = 0.725$. The right panel shows the source plane reconstruction for images 2.1. Overlaid are the caustic curve originated from the cluster-scale clump (blue) and the galaxy GAL1 (red), delineating three regions of image multiplicity.

the systems 1 and 2) can only be reproduced using a bimodal mass distribution. Indeed, we find that a model with 2 cluster clumps *DM1* and *DM2* fixed at the locations of the two brightest cluster galaxies gives a much better σ_i ($2.2''$). Thanks to the larger number of identified multiple images systems, we can allow the centers (α_1, δ_1) and (α_2, δ_2) of each clump to vary.

In addition, the shape and location of the 5 images previously identified in the giant arc (System 2) are strongly influenced by the nearby cluster galaxies. This is particularly

true for the galaxy GAL1 (Fig 1) which distorts the circular shape of the arc, and the BCG at the south hand side of the cluster. To better reproduce the giant arc, we choose to model these two galaxies with two independent dPIE potentials. In total, the new model contains 24 free parameters and we have 40 constraints from the multiple images. The resulting σ_i of this model is $\sim 1.76''$, which is good compared to other similar works (Limousin et al. 2007; Richard et al. 2009a). We adopt this model as our best-fit model for the rest of this letter. The parameters of this model as well as

Table 1. Properties of the multiple imaged systems. Redshift values quoted with brackets are predictions from the lensing model.

Multiple	α	δ	F814W–F475W	F814W–F625W	F814W	z
1.1	39.966857	-1.5769063	-1.08 ± 0.13	-0.66 ± 0.10	23.04 ± 0.06	0.806
1.2	39.976088	-1.5760316	-0.93 ± 0.17	-0.66 ± 0.14	23.88 ± 0.08	0.806
1.3	39.968466	-1.5766097	-1.11 ± 0.13	-0.77 ± 0.10	22.96 ± 0.06	
2.1	39.973639	-1.5842121	-2.61 ± 0.24	-1.13 ± 0.08	21.81 ± 0.05	0.725
2.2	39.970772	-1.5850722	-2.54 ± 0.17	-1.04 ± 0.06	21.48 ± 0.05	0.725
2.3	39.968546	-1.5845042	-2.65 ± 0.15	-1.07 ± 0.06	20.88 ± 0.05	0.725
2.4	39.969185	-1.5847126	-2.65 ± 0.15	-1.07 ± 0.06	20.88 ± 0.05	0.725
2.5	39.969421	-1.5848306	-2.20 ± 0.09	-0.55 ± 0.06	21.88 ± 0.05	0.725
3.1	39.965457	-1.5668639	0.31 ± 0.23	0.39 ± 0.22	24.08 ± 0.18	[1.59±0.07]
3.2	39.968333	-1.5658229	0.19 ± 0.25	0.52 ± 0.21	24.05 ± 0.18	
3.3	39.977084	-1.5671820	0.00 ± 0.37	0.28 ± 0.35	25.16 ± 0.25	
4.1	39.979437	-1.5763194	-0.03 ± 0.18	0.05 ± 0.18	24.37 ± 0.13	[1.26±0.03]
4.2	39.970545	-1.5762639	0.02 ± 0.21	-0.01 ± 0.22	24.38 ± 0.15	
4.3	39.961736	-1.5779306	-0.08 ± 0.27	-0.15 ± 0.28	24.81 ± 0.18	
5.1	39.973275	-1.5890694	-0.30 ± 0.36	-0.41 ± 0.38	24.69 ± 0.21	[1.28±0.03]
5.2	39.970954	-1.5892361	-0.78 ± 0.55	-0.45 ± 0.19	23.53 ± 0.16	
5.3	39.968620	-1.5890278	-0.46 ± 0.30	-0.71 ± 0.36	23.93 ± 0.16	
6.1	39.969266	-1.5771944	-2.32 ± 0.72	-1.39 ± 0.31	23.17 ± 0.09	[1.06±0.02]
6.2	39.964320	-1.5782500	-2.75 ± 0.87	-1.56 ± 0.47	22.66 ± 0.08	
6.3	39.979437	-1.5771388	-2.60 ± 0.44	-1.69 ± 0.33	22.46 ± 0.08	
7.1	39.969579	-1.5804097	-0.56 ± 0.09	-0.18 ± 0.08	23.03 ± 0.06	[1.78±0.25]
7.2	39.969673	-1.5807406	-0.46 ± 0.38	-0.16 ± 0.31	24.97 ± 0.20	
7.3	39.968606	-1.5856111	-0.89 ± 0.45	-0.23 ± 0.30	24.85 ± 0.20	
7.4	39.961367	-1.5800139	-0.64 ± 0.30	0.04 ± 0.18	24.54 ± 0.10	
7.5	39.983602	-1.5779652	-0.48 ± 0.52	-0.23 ± 0.43	25.54 ± 0.26	
8.1	39.964292	-1.5697917	-0.20 ± 0.54	0.36 ± 0.42	25.91 ± 0.33	[2.41±0.22]
8.2	39.961680	-1.5736806	-0.35 ± 0.43	-0.57 ± 0.68	25.68 ± 0.33	
8.3	39.983911	-1.5733471	-0.15 ± 1.50	0.00 ± 1.98	26.98 ± 1.34	
9.1	39.962215	-1.5778958	0.40 ± 0.74	-0.22 ± 0.99	27.41 ± 0.59	[1.54±0.06]
9.2	39.969287	-1.5762569	0.28 ± 1.34	0.44 ± 1.27	27.47 ± 1.03	
9.3	39.981833	-1.5765536	0.04 ± 0.49	-0.02 ± 0.50	26.37 ± 0.34	
10.1	39.968189	-1.5714444	0.10 ± 0.47	0.50 ± 0.41	26.05 ± 0.35	

their 1σ errors are given in Table 2. The predicted redshifts for systems 3 to 9 are presented in Table 1. We note that the large majority of them are about $z \sim 1$. Such a redshift overdensity is often seen when looking at lensed fields.

Although the value of σ_0 for *DM2* is a lot higher than for *DM1*, r_{core} for *DM2* is also much larger, and therefore the total masses of each cluster-scale component are similar. Thanks to the proximity of GAL1 to images 2.3, 2.4 and 2.5 (see Fig. 1), we obtain tight constraints on its parameters σ_1 and $r_{cut,1}$ (Table 2). Interestingly, we find very little difference between the constrained values ($\sigma_1 = 118$ km/s, $r_{cut,1} = 20$ kpc) and the values it would have had if scaled according to its luminosity $0.17 L^*$ ($\sigma'_1 = 123$ km/s, $r'_{cut} = 18$ kpc).

4 RESULTS

We use the best-fit model to unlens the giant arc to the source plane. Fig. 1 shows that the source morphology resembles a local spiral galaxy with a red bulge, blue spiral arms containing individual knots of star formation. We also overlay the location of the cluster-scale and GAL1 caustic

lines at the giant arc redshift $z = 0.725$. They part the source into 3 regions of different multiplicity. The eastern part of the source lies outside of both caustics and is singly imaged, the western part inside the cluster caustic is triply imaged, while the central red bulge inside both caustics is a system of 5 images, as we identified earlier from the HST image. The reconstruction of each part of the giant arc agrees with this source-plane morphology. Intrinsically, the source extends $10.0 / 2.5$ kpc along its major/minor axis, and assuming a disk-like morphology it is observed with an inclination of 75 degrees. By comparing the overall fluxes in the image and the source plane, we derive a total magnification of 32 ± 4 for the entire arc. The largest linear magnification is obtained for image 2.2, where the centre is resolved at < 50 pc.

The reconstructed mass distribution (Fig. 2) shows two main peaks located over the two brightest cluster galaxies. The center of *DM1* is located within $1''$ of the BCG, while a significant offset (about $10''$, or 50 kpc) separates the center of *DM2* from the second BCG to the north. This offset is well constrained by the presence of multiple systems on both northern and southern directions. Such a large offset between the dark matter component and the stellar light is not unusual, as a similar value of $\sim 9''$ was found in the case of

Table 2. Best fit parameters of the mass models. Values in brackets are not optimized.

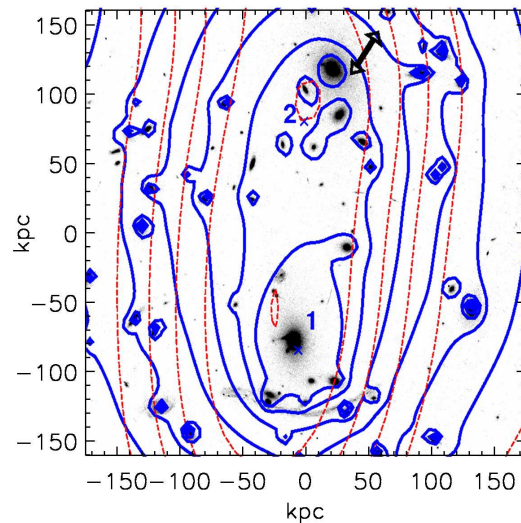
Comp.	x [$''$]	y [$''$]	e	θ [deg]	σ_0 [km/s]	r_{core} kpc	r_{cut} kpc
DM1	1.2 ± 0.2	-0.6 ± 0.6	$0.26^{+0.10}_{-0.06}$	-11 ± 4.0	596 ± 30	$30.2^{+3.3}_{-0.2}$	[800]
DM2	1.5 ± 0.2	27.3 ± 1.0	$0.31^{+0.02}_{-0.03}$	-6.1 ± 0.6	1316 ± 35	123^{+8}_{-4}	[800]
BCG	[0.0]	[0.0]	[0.30]	[-81.9]	194 ± 30	[0.14]	43 ± 5
GAL1	[7.9]	[-9.8]	[0.26]	[25.7]	118 ± 13	[0.06]	20 ± 6
L*					193 ± 9	[0.15]	[45]

Abell 1689 (Limousin et al. 2007). We also observe that the orientation of the northern radial arc (System 10), which was *not* explicitly included as a strong lensing constraint, is fully consistent with the location of *DM2*, rather than with the center of the northern BCG (Fig. 2). Finally, we note that the model in which the centers of *DM1* and *DM2* are fixed at the positions of the respective BCGs (see Sect. 3) requires a very large and unrealistic ellipticity for the secondary clump ($e \sim 0.6 - 0.7$).

The mass enclosed within a radius of 250 kpc from the barycenter of the mass distribution (located halfway between the centers of *DM1* and *DM2*) is $3.8 \pm 0.2 \cdot 10^{14} M_{\odot}$. We find a good agreement (within 3σ) when deriving the same mass using the NFW fit of the Subaru weak-lensing measurements from Broadhurst et al. (2008): $M_{WL} = 4.3 \cdot 10^{14} M_{\odot}$. The statistical error on the enclosed mass is always better than 5% within a radius of $100''$, which is a significant improvement compared to the model of Kneib et al. (1993) who found typical errors of $\sim 15\%$. Then, we estimated the *effective* Einstein radius θ_E , defined for a source at $z = 2.0$, as the radius at which the averaged convergence $\kappa(< \theta_E) = 1$ (see Broadhurst & Barkana 2008; Richard et al. 2009a). By computing it from the barycenter of the mass distribution, we find $\theta_E = 39'' \pm 2''$. The enclosed mass within θ_E is $2.82 \pm 0.15 \cdot 10^{14} M_{\odot}$. This large Einstein radius makes Abell 370 one of the best clusters to be used as a *gravitational telescope* to search for very distant galaxies, similar to other clusters such as A1689 (Broadhurst et al. 2005), A1703 (Richard et al. 2009a) or MACS0717 (Zitrin et al. 2009). Indeed, we outline in Fig. 1 the boundary of the region where multiple images happen for a source at very high redshift ($z = 6$), and show that it can assimilate to a circular region of $\sim 50''$ radius.

In Fig. 2, we overlay the X-ray luminosity contours on top of the mass distribution contours, and observe a very good match. In particular, the contours share a similar elliptical shape and the same orientation. We use the `ellipse` IRAF task to quantify the typical ellipticity e and position angle θ of these contours, and measure ($e = 0.60, \theta = -6^\circ$) and ($e = 0.62, \theta = -5^\circ$) for the dark matter and X-ray maps, respectively, confirming the very good morphological agreement. Like the mass distribution, the X-ray luminosity map shows evidence for two prominent maxima, located near the dark matter clumps, with an offset smaller than $10''$.

Overall, the galaxy distribution, the mass distribution and the X-ray luminosity map each present two consistent peaks, and suggest that we are witnessing a massive cluster during a phase of merging. Only two other clusters have shown such a bimodality with two peaks of dark matter and X-ray: the *bullet cluster* (Bradač et al. 2006, 2009), and

**Figure 2.** Total mass (blue solid) and X-ray (red dashed) linearity-spaced contours overlaid on top of the HST image. The centers of the cluster-scale clumps are marked with 1 and 2, and the orientation of the radial arc system 10 is indicated by a double arrow.

MACS0025 (also known as the *baby bullet*, Bradač et al. 2008b). The main difference between these two clusters and Abell 370 is that both show much larger offsets (of the order of 200-350 kpc) between the X-ray and dark matter centers on each peak. Therefore it seems that the smaller offsets in Abell 370 are due to a projection effect, or due to the fact that the cluster is seen in an earlier stage of the merging process, at a time when the merging process has not yet affected much the baryons in the ICM.

Looking at the dynamical information on Abell 370, de Filippis et al. (2005) have measured the redshift distribution of cluster galaxies, and shown that the redshift distribution has two redshift peaks separated by ~ 3000 km/s in velocity, with each of the two brightest galaxies belonging to a different redshift group. This suggests that contrary to the case of the bullet cluster and MACS0025, the merging of the two cluster components has a large projected velocity along the line of sight, which partly explains the smaller offsets observed between the X-ray and dark matter peaks.

ACKNOWLEDGMENTS

We are very grateful to the astronauts who made the service mission SM4 a scientific success, and to K.Noll, R.Lucas and their team who have conducted this spectacular ERO observation. We acknowledge useful discussions with Mark

Swinbank. JR acknowledges support from an EU Marie-Curie fellowship. JPK acknowledges support from the CNRS, the Agence Nationale de la Recherche grant ANR-06-BLAN-0067, and the French-Israelian collaboration project 07-AST-F9. ML acknowledges the CNES and CNRS for their support. The Dark Cosmology Centre is funded by the Danish National Research Foundation. Results are based on observations made with the NASA/ESA Hubble Space Telescope.

REFERENCES

- Abdelsalam H. M., Saha P., Williams L. L. R., 1998, *MNRAS*, 294, 734
- Bergmann A. G., Petrosian V., Lynds R., 1990, *ApJ*, 350, 23
- Bézecourt J., Kneib J. P., Soucail G., Ebbels T. M. D., 1999, *A&A*, 347, 21
- Bouwens R. J., et al., 2009, *ApJ*, 690, 1764
- Bradač M., et al., 2006, *ApJ*, 652, 937
- , 2008a, *ApJ*, 681, 187
- , 2008b, *ApJ*, 687, 959
- , 2009, *astro-ph/0910.2708*
- Broadhurst T., et al., 2005, *ApJ*, 621, 53
- , 2008, *ApJ*, 685, L9
- Broadhurst T. J., Barkana R., 2008, *MNRAS*, 390, 1647
- Coe D., et al., 2008, *ApJ*, 681, 814
- de Filippis E., Sereno M., Bautz M., 2005, *ASR*, 36, 715
- Ebeling H., White D., Rangarajan F., 2006, *MNRAS*, 368, 65
- Elíasdóttir Á., et al., 2007, *astro-ph/0710.5636*
- Golse G., Kneib J.-P., 2002, *A&A*, 390, 821
- Jullo E., et al., 2007, *New Journal of Physics*, 9, 447
- Jullo E., Kneib J., 2009, *MNRAS*, 395, 1319
- Kneib J.-P., 1993, Ph.D. Thesis
- Kneib J.-P., Ellis R. S., Smail I., Couch W. J., Sharples R. M., 1996, *ApJ*, 471, 643
- Kneib J. P., Mellier Y., Fort B., Mathez G., 1993, *A&A*, 273, 367
- Limousin M., et al., 2007, *ApJ*, 668, 643
- , 2008, *A&A*, 489, 23
- Lynds R., Petrosian V., 1986, in *Bull. of the Am. Astron. Soc.*, Vol. 18, pp. 1014–+
- Richard J., et al., 2008, *ApJ*, 685, 705
- , 2009b, *arXiv:astro-ph/0911.3302*
- Richard J., Pei L., Limousin M., Jullo E., Kneib J. P., 2009a, *A&A*, 498, 37
- Smail I., et al., 1996, *ApJ*, 469, 508
- Smith G. P., et al., 2005, *MNRAS*, 359, 417
- Soucail G., Fort B., Mellier Y., Picat J. P., 1987, *A&A*, 172, L14
- Soucail G., Kneib J., Golse G., 2004, *A&A*, 417, L33
- Soucail G., Mellier Y., Fort B., Mathez G., Cailloux M., 1988, *A&A*, 191, L19
- Swinbank M., et al., 2009, *astro-ph/0909.0111*
- Zitrin A., Broadhurst T., 2009, *ApJ*, 703, L132
- Zitrin A., Broadhurst T., Rephaeli Y., Sadeh S., 2009, *astro-ph/0907.4232*
- Zitrin A., et al., 2009, *MNRAS*, 396, 1985